IOP Publishing Journal of Micromechanics and Microengineering
J. Micromech. Microeng. **30** (2020) 125013 (11pp) https://doi.org/10.1088/1361-6439/abbf89

Shoulder fillet effects in strength distributions of microelectromechanical system components

Frank W DelRio[1,2], Brad L Boyce[2], Jake T Benzing[1], Lawrence H Friedman[3] and Robert F Cook[3]

[1] Material Measurement Laboratory, National Institute of Standards and Technology, Boulder, CO 80305, United States of America
[2] Sandia National Laboratories, Material, Physical, and Chemical Sciences Center, Albuquerque, NM 87185, United States of America
[3] Material Measurement Laboratory, National Institute of Standards and Technology, Gaithersburg, MD 20899, United States of America

E-mail: fwdelri@sandia.gov

Received 31 July 2020, revised 8 September 2020
Accepted for publication 8 October 2020
Published 6 November 2020

Abstract

The failure forces and fracture strengths of polysilicon microelectromechanical system (MEMS) components in the form of stepped tensile bars with shoulder fillets were measured using a sequential failure chain methodology. Approximately 150 specimens for each of four fillet geometries with different stress concentration factors were tested. The resulting failure force and strength distributions of the four geometries were related by a common sidewall flaw population existing within different effective stressed lengths. The failure forces, strengths, and flaw population were well described by a weakest-link based analytical framework. Finite element analysis was used to verify body-force based expressions for the stress concentration factors and to provide insight into the variation of specimen effective length with fillet geometry. Monte Carlo simulations of flaw size and location, based on the strength measurements, were also used to provide insight into fillet shape and size effects. The successful description of the shoulder fillet specimen strengths provides further empirical support for application of the strength and flaw framework in MEMS fabrication and design optimization.

Keywords: strength distributions, flaw populations, polysilicon microelectromechanical system, shoulder fillets, fracture

(Some figures may appear in colour only in the online journal)

1. Introduction

A core function of engineering mechanics is to translate limited coupon-level material test data into accurate predictions of the load bearing ability of components in novel shapes and sizes. For economic reasons, such predictions are usually based on measurements of test coupons or test components much simpler in shape, smaller in size, or fewer in number than those manufactured for commercial application. For microelectromechanical systems (MEMS) in particular, prediction of the mechanical performance and reliability of the many billions of manufactured MEMS devices [1] thus entails significant leverage of information from, at most, thousands of test components sampled and measured to make such predictions [2]. Thus, prediction of the load bearing ability of MEMS requires clear quantitative relationships between the mechanical properties of the materials forming the components and the shape and size of the components. The majority of MEMS devices are fabricated from polycrystalline silicon (polysilicon) and hence the relevant material property for load bearing assessment is brittle fracture strength [3–6]. An extensive review of MEMS-related silicon strength [7] showed that the

qualitative factors controlling polysilicon fracture strengths are well understood, such that the relevant processing-structure-property relationships are well established. However, the review also suggested that although there were many quantitative measurements of failure loads, interpreted as material strengths for simple shapes and sizes of components, quantitative, predictive, materials property-performance relationships were largely absent. Therefore, optimized component design, manufacturing yield, and operational reliability predictions for MEMS are significantly impeded. The work here addresses this issue by validating a recently developed probabilistic flaw-sampling model [8–10] using the fracture strengths of a set of MEMS test components with a range of stress-concentrating features.

In common with single-crystal silicon, polysilicon is brittle, and the fracture strength σ_f is controlled by flaws [7, 11]: the larger the flaw, the smaller the strength. In some brittle materials, strength-controlling flaws are cracks associated with material and elastic discontinuities such as bulk pores or surface roughness [12], and in others, flaws are the residual deformation and cracks generated on surfaces by elastic-plastic contacts and scratches. Detailed analyses have been developed in recent work [8, 9] considering the relationships between component strength distributions and underlying elastic and elastic-plastic flaw size populations in bulk ceramics, silicon dies, MEMS, and nanowires. The strength-controlling flaws in polysilicon MEMS are usually sub-μm-scale roughness or grain boundaries grooves on component sidewalls. As a component is loaded, tensile stress concentrations develop in zones at the base of the grooves, particularly deep grooves, driving crack initiation and propagation. Under uniform far-field stress, the largest flaw or most potent groove-crack combination becomes unstable at the smallest applied load and therefore determines the strength of the component. The details of fabrication determine flaw population in a material in terms of the distribution of groove sizes and their spatial density on the sidewalls, thus determining the strength distribution for a group of components. The probabilistic flaw-sampling analyses have been applied in the deconvolution of strength measurements of two different shaped MEMS components—notched tensile bars and uniform tensile bars—to determine the size distribution and spatial density of flaws in MEMS as a function of position in the MEMS fabrication stack [10].

In the study here, the recent work is extended to assess strength measurements of polysilicon MEMS components with a range of different stress concentrating features—four stepped tensile bars characterized by different shoulder fillets. The study has many features in common with the previous work [10]: (1) All components were formed in the same MEMS fabrication sequence, such that the strength-controlling flaws in each component are drawn from the same population; (2) A different stress concentration factor (SCF) K_t was used for each different macroscopic component shape, on which the common microscopic surface flaw population is superposed; (3) The failure force F_f for each component was determined using a sequential failure chain geometry; and (4) The flaw population was characterized by two intensive attributes, a probability density function (pdf), the intensive flaw size pdf $f(c)$, where c is the flaw characteristic length dimension, and a mean separation of flaws on a sidewall ΔL, where $1/\Delta L$ is the mean spatial density/length. In addition to extending the applicability and confidence in the previous methodology, the results herein reinforce the different engineering aspects of MEMS device fabrication. In MEMS design, the extensive, size-dependent properties of MEMS components (e.g. F_f) govern the performance of a MEMS device. In MEMS manufacturing, the intensive, size-independent properties of MEMS materials (e.g. $f(c)$ and ΔL) are determined by MEMS processing. The extensive and intensive properties are related by component geometry (e.g. relative dimensions determine K_t and length determines number of flaws). It is the goal of this work to advance MEMS design capabilities by establishing a clear connection between the extensive *and* intensive properties of MEMS components, thus facilitating specification of the load bearing ability of components with arbitrary geometry.

2. Materials and methods

2.1. Specimen design and fabrication

The sequential failure chain concept for high-throughput tensile testing of MEMS components has been depicted elsewhere [2]. Briefly, 20 test specimens are connected in series, forming a slack chain. One end of each specimen is fixed to the substrate, while the other end is connected to the remainder of the chain through a series of linkage elements. A force F_{app} is initially applied to the free end of the chain. The force is at first only supported by the first tensile specimen (figure 1(a), top). F_{app} is increased until fracture of this first specimen and slack is then taken up in the first linkage element and F_{app} is transferred to the second tensile specimen (figure 1(a), middle). F_{app} is increased again until fracture of the second specimen and slack is taken up by the second linkage element (figure 1(a), bottom). This process is repeated sequentially until all specimens in the chain are broken. In this method, ≈1000 specimens can be independently, sequentially, and unambiguously tested in ≈16 h.

An array of slack-chain tensile specimens was fabricated using the SUMMiT V™ process flow (reticle set RS723); a scanning electron microscopy (SEM) image of several completed chains is shown in figure 1(b). The fabrication process entailed depositing, patterning, and etching four polysilicon layers separated by three sacrificial silicon dioxide layers; in this study, the tensile specimens were formed only in the third polysilicon layer (poly3), such that the layer-to-layer strength variability observed in previous studies was eliminated [4, 10]. Individual die were then released using an HF-based etchant, dried using a super-critical CO_2 procedure, and coated with a silane-based anti-stiction monolayer [13]. Four different test specimen geometries were formed in the poly3 layer, each with a different maximum width D, minimum width d, and shoulder radius r as shown in figures 1(c)–(f). The specimen names and nominal dimensions (D, d) for the four shoulder fillet geometries were S1 (20 μm, 2 μm), S2 (4 μm, 2 μm),

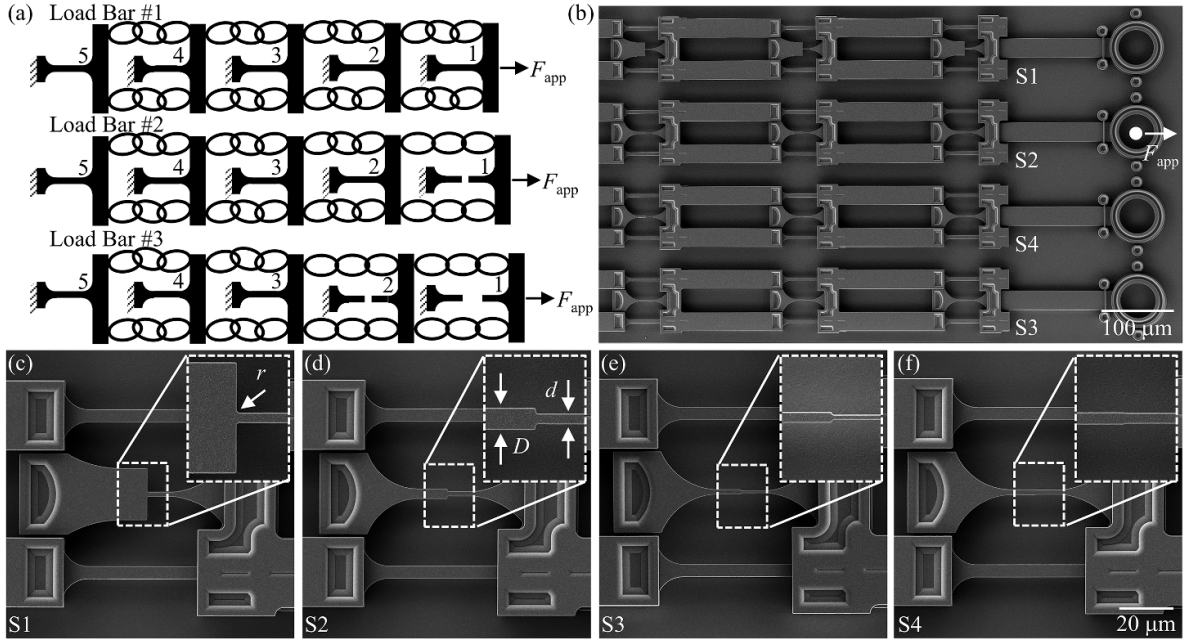

Figure 1. Specimen design and fabrication. (a) Schematic representation of the slack-chain concept for high-throughput tensile testing. (b) SEM image of completed chains fabricated using the SUMMiT V™ process. (c)–(f) High-resolution SEM images of the four different specimen geometries before testing, each with a different *D, d*, and *r* as shown in the insets.

S3 (2 μm, 1 μm), and S4 (2.25 μm, 2 μm). All geometries were designed with 90° angles at the interface between the maximum and minimum widths, such that the ensuing *r* were dictated by the fabrication process. The length *L* of each specimen was ≈20 μm and the shoulder fillets were located in the middle of the gauge region. The nominal thickness *h* of the poly3 layer was 2.25 μm. All specimens were fabricated in a single reticle set, ensuring that the microscopic features (i.e. $f(c)$ and ΔL) remained invariant as the macroscopic shape (i.e. *D, d*, and *r*) was changed.

2.2. Strength testing

Strength testing was performed by extending the pull-tab ring at the end of each chain with a custom-built MEMS mechanical probe station and recording applied force F_{app} as a function of time *t* [2, 4]. The mechanical probe station is depicted schematically in figure 2(a) and pictorially in figure 2(b). The MEMS test structures, typically located on a 3 mm × 8 mm die, were centered under the probe station on an aluminum sample stage with a vacuum chuck. The sample stage was in turn fixed to a two-axis motion controller to facilitate horizontal movement of the stage and sample with respect to an optical microscope fixed in the station; the microscope included long working-distance lenses and a camera. An independent three-axis motion controller with 0.1 μm resolution linear displacement encoders was fixed to the sample stage and used as the drive actuator for mechanical testing. External force sensing was performed using a 1 N load cell with 6 μN force resolution. A tungsten probe was attached to the end of the load cell to engage the pull-tab rings. The probe tip was machined with a focused ion beam tool into a cylindrical geometry (inset in figure 2(a)). The probe-tip diameter was designed to be slightly smaller than the pull-tab diameter to enable a robust connection to the rings. The probe-tip end was designed to be flat and parallel to the die surfaces to eliminate frictional forces observed in previous designs [14]. All probe station functionality was directed via custom software.

A typical F_{app}-*t* trace obtained by the mechanical probe station is shown in figure 2(c) and examples of failed S1 to S4 specimens are shown in figures 2(d)–(g). In most cases, only the first 18 or 19 tensile tests were conducted, such that the chain remained connected to the substrate after testing. F_f was taken to be the maximum force for each specimen trace just prior to fracture. The stress in the small gauge section at fracture σ_g is given by $\sigma_g = F_f/(dh)$, where *dh* is the cross-sectional area of the minimum width. It is important to note that $\sigma_g \neq \sigma_f$. The shoulder fillets in each specimen locally enhanced the stress to values greater than that in the small gauge. The enhancement is characterized by a SCF, K_t. As such, σ_f was calculated by $\sigma_f = K_t F_f/(dh)$, where K_t was determined from the shoulder fillet dimensions and SCF equations obtained by the body force method [15, 16]. The advantage of using numerical SCF equations [16] over conventional SCF tables [17] is the ability of equations to assess K_t for any fillet geometry. The uncertainties in K_t from dimensional dispersions were a few percent of the mean values, comparable to the errors in the numerical solutions for K_t [16].

The number of strength tests *N* in each group of specimens of different geometry varied from 133 to 170 as shown in table 1. The F_f, σ_g, and σ_f data were used to form empirical distribution functions (edfs) for each of the component geometries. F_f,

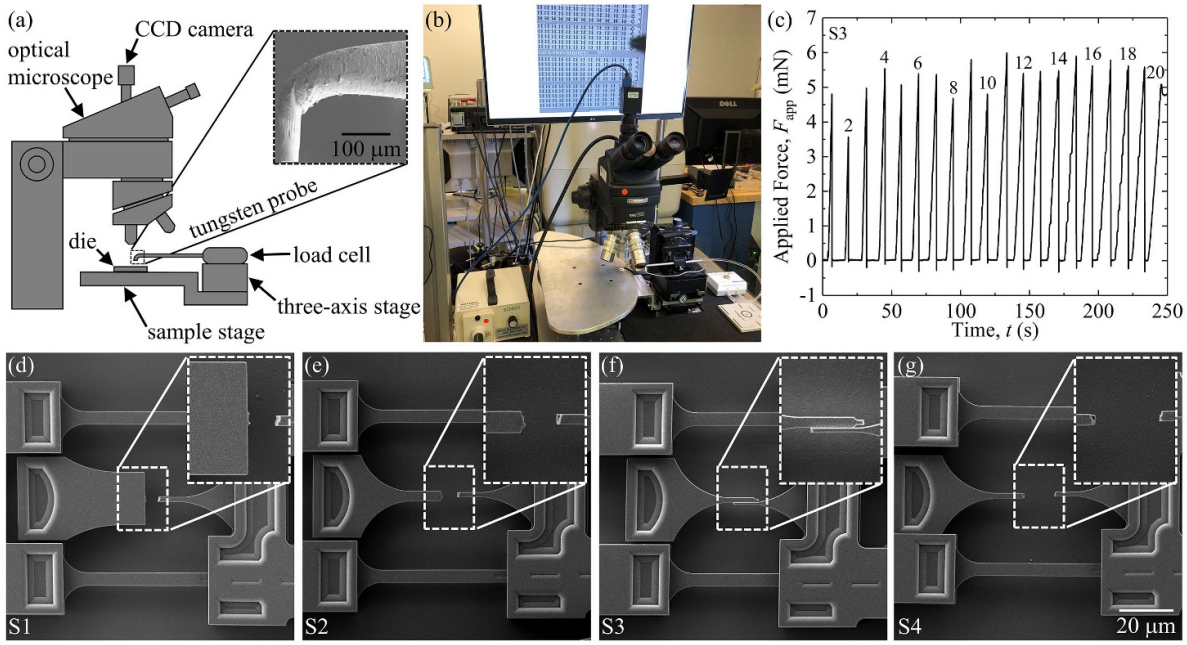

Figure 2. Mechanical probe station and strength testing. (a) Schematic representation and (b) picture of the custom-built MEMS mechanical probe station. (c) Typical F_{app}-t profile for 20 sequential tests; F_f was taken to be the maximum force of each trace just before fracture. (d)–(g) High-resolution SEM images of the four different specimen geometries after testing, each depicting failure at or near the shoulder fillet region as shown in the insets.

Table 1. Number of specimens, maximum widths, minimum widths, and shoulder radii for the four shoulder fillet geometries. Uncertainty values are one standard deviation of the mean from at least ten specimens.

Specimen Type	Number of Specimens, N	Maximum Width, D (μm)	Minimum Width, d (μm)	Shoulder Radius, r (μm)
S1	133	19.32 ± 0.06	1.91 ± 0.02	0.54 ± 0.02
S2	162	3.85 ± 0.03	1.90 ± 0.03	0.55 ± 0.03
S3	170	1.89 ± 0.03	0.90 ± 0.02	0.58 ± 0.02
S4	153	2.14 ± 0.02	1.89 ± 0.02	3.04 ± 0.04

σ_g, and σ_f in each group were ranked from smallest to largest, such that i was the rank value and $P_i = (i - 0.5)/N$ was the rank parameter. The discrete functions $P(F_f)$, $P(\sigma_g)$, and $P(\sigma_f)$ for each geometry were group-specific edfs, providing discrete estimates of the continuous cumulative distribution functions (cdfs) sampled from the larger material population.

2.3. Strength distribution and flaw population analysis

$P(\sigma_f)$ for each group was fit with the continuous and bounded sigmoidal smoothing function

$$F(\mu) = 30\left[\left(\mu^{3p}/3\right) - \left(\mu^{4p}/2\right) + \left(\mu^{5p}/5\right)\right], \qquad (1)$$

where

$$\mu = (\sigma - \sigma_{min}) / (\sigma_{max} - \sigma_{min}) \qquad (2)$$

is the relative strength position within the $F(\mu)$ domain [9]. σ_{min} and σ_{max} are empirical fitting parameters that define the lower and upper limits of the smoothing domain and p represents an empirical fitting parameter of order unity that controls the sigmoid symmetry. The key benefits of equations (1) and (2) over other smoothing functions such as the Weibull description include boundedness at the limits ($F(0) = 0$, $F(1) = 1$, $F'(0) = F'(1) = 0$) and separation of shape from the properties of the bounds (p changes the shape of the sigmoid independently of σ_{min} and σ_{max}) [9]. It is important to note that σ_{min} and σ_{max} are group-specific parameters that vary with component size, geometry, and loading, in contrast to the intensive characteristics of threshold strength σ_{th} and upper limit strength σ_u of the overall strength population. However, if the number of strength-limiting flaws in a component k is small ($k \to 1$) and the number of strength tests N is large ($N \to \infty$), the group-specific parameters converge to the population-invariant intensive parameters ($\sigma_{min} \to \sigma_{th}$, $\sigma_{max} \to \sigma_u$). Thus, high-throughput testing of components with notches or fillets (i.e. components with large SCF that limit the failure location to a small area) can be used to assess the flaw-size pdf $f(c)$.

The $P(\sigma_f)$ functions for each group given by equations (1) and (2) were used to estimate the flaw-size pdf $f(c)$ and flaw spacing ΔL. For the flaw-size pdf $f(c)$, $F(\mu)$ can be related to the intensive flaw-size cdf $F(c)$ by

$$F(c) = [1 - F(\mu)]^{\Delta L/L}, \tag{3}$$

where (as defined above) ΔL is the spatial separation of flaws in the *population* and L is the length of the specimens in the *group* [8, 9]. It is noted that the ratio $L/\Delta L$ gives the average number of flaws/specimen, $L/\Delta L = k$, and that $F(c)$ and $F(\mu)$ are related by this ratio, equation (3). For the double edge-notched specimens previously, $k = 2$ was used in equation (3), as specimen failure was determined by the two strength-controlling sidewall flaws at each notch root [10]. In implementing equation (3) here, $k = 2$ is also used for the S1 data, consistent with the expectation that specimen failure is determined by the two strength-controlling sidewall flaws at each shoulder with large SCF [4, 5, 10]. The usage of equation (3) requires a relationship between strength and flaw size, here taken to be the Griffith equation

$$\sigma = Bc^{-1/2}, \tag{4}$$

where B is a constant involving toughness, set by the material, and flaw geometry and residual stress state, set by the manufacturing process [18]. Recent work concluded that the nature of the flaws occurring as polysilicon component sidewall features was somewhat different than simple Griffith cracks [10], and was consistent with both small, rounded grooves with no discernable crack tip [4, 5] and small cracks at the roots of rounded grooves [19]. Inclusion of more complex flaw geometries can be incorporated into the analytical framework through modifications to the Griffith equation via different power-law relationships for strength, but come with the added burden of finite element calculations and experimental data on the groove dimensions. Once the intensive cdf $F(c)$ is determined, $f(c)$ can be obtained from

$$f(c) = dF(c)/dc. \tag{5}$$

In this case, $F(c)$ was estimated from a fit of $F(\mu)$ to the experimental data from the S1 specimens.

To determine flaw spacing ΔL, equation (3) was extended to consider two specimen groups of different lengths L_1 and L_n. The groups were sampled from the same flaw population $f(c)$, but revealed different strength distributions $F_1(\mu)$ and $F_n(\mu)$, such that the flaw-size cdfs for the groups were given by

$$F(c) = [1 - F_1(\mu)]^{\Delta L/L_1} \tag{6}$$

and

$$F(c) = [1 - F_n(\mu)]^{\Delta L/L_n}. \tag{7}$$

The two flaw-size cdfs in equations (6) and (7) were then combined to eliminate ΔL to arrive at

$$F_n(\mu) = 1 - [1 - F_1(\mu)]^{(L_n/L_1)}. \tag{8}$$

This relationship enabled distribution $F_1(\mu)$ from specimens of length L_1 to define distribution $F_n(\mu)$ from specimens of length L_n via the length scaling factor L_n/L_1, where $n = 2$, 3, and 4 for specimens S2, S3, and S4. More specifically, equation (8) was fit to the strength data for the S2, S3, and S4 specimens using the fit for the S1 specimens from equation (1) as a basis and L_2/L_1, L_3/L_1, and L_4/L_1 as the fitting parameters. In previous work on notched and tensile specimens [10], the experimentally determined length scaling factors $L_{\text{tensile}}/L_{\text{notch}}$ were used to assess ΔL through the relation $\Delta L = (20L_{\text{notch}}/L_{\text{tensile}})$ μm, which was established by recognizing that $L_{\text{notch}} = 2\Delta L$ for the notched specimens and $L_{\text{tensile}} = 40$ μm for the tensile specimens. However, there are no specimen geometries in this work with defined lengths over which the flaw population is active (i.e. tensile specimens), precluding the direct assessment of ΔL from the length scaling factor. Instead, ΔL measurements for the poly3 layer from previous work were used for comparison with stress distribution diagrams from finite element analysis (FEA) simulations around the shoulder fillet regions and to generate scaled diagrams of specimens. The diagrams enabled a quantitative comparison of the spatial separation of surface flaws and the spatial extent of the stress fields.

2.4. Monte Carlo simulations

The quantitative characteristics of the flaw size distribution and mean spacing of the flaw population, $f(c)$ and ΔL, were used to simulate the surfaces of the shoulder fillet regions via Monte Carlo methods. The flaw sizes were selected randomly from $f(c)$ as assessed from S1 specimens. The flaw spacings were sampled from a uniform ΔL distribution with a mean of 0.57 μm and range of $\pm$ 0.48 μm about the mean; this distribution is consistent with the mean spacing and uncertainty for the poly3 layer as determined in previous work [10]. The outlines of the specimens were described by piecewise continuous arc and straight sections matched to the fillet radii and gauge widths of the S1 and S2 specimens and by single continuous functions matched to the fillet lengths and gauge widths of the S3 and S4 specimens. Specimen dimensions in the schematic diagrams are to scale. The flaws are denoted as straight lines and omitted from non-tensile surfaces. Many simulations were conducted and those presented are typical.

2.5. FEA simulations

FEA on the S1 to S4 geometries was performed using ABAQUS [20]. The specimen lengths were chosen to provide *far field* loading conditions of uniform tensile stress; the maximum and minimum width sections had lengths 5$\times$ larger than their respective widths. The specimens were also treated as plate-like with small deformations; linear plane-stress constitutive laws were used here, such that the results are directly comparable to the body force method results from previous work [16]. The maximum width sections were fixed axially, but unconstrained laterally to allow for Poisson contractions. The minimum width sections were loaded axially with unit stress so the maximum principal stress contours were identical to SCFs. Adaptive meshing of second-order triangles (CPS6 elements) verified that models converged to 0.1% using the

representative von Mises stress error. von Mises error is not physically relevant to brittle fracture, but it is numerically relevant as it quantifies overall stress error for multiaxial stress states. Local SCFs were plotted for the S1 to S4 geometries.

3. Results

3.1. Specimen geometry and fracture behavior

The specimen geometries resulting from fabrication were characterized using high-resolution SEM images (insets in figures 1(c)–(f)) of the shoulder fillets prior to mechanical testing. The mean values and standard deviations for D, d, and r from analysis of at least ten specimens are given in table 1. From the mean values, it was revealed that D and d were slightly less than the nominal values for S1 to S4; the systematic decrease in both dimensions was due to a linewidth loss of $\approx$0.05 μm per edge during etching. Moreover, the SEM images showed that r were similar for S1 to S3 but increased markedly for S4; the deviation for S4 was likely due to an inability to obtain small r with similar D and d during patterning. Interestingly, the radii presented herein for polysilicon were significantly larger than those in previous work for single-crystal silicon [21], despite both studies using sharp 90° corners in their respective designs. The differences in r were due to the disparate fabrication processes; the polysilicon components were formed via reactive ion etching, whereas the single-crystal silicon components were formed by anisotropic etching of epitaxial silicon. From the standard deviations, it was demonstrated that the dimensional dispersions were only a few percent of the mean values and akin to sidewall surface roughness. The roughness is due to etching or grain boundary grooving during thermal and chemical steps in the fabrication process and gives rise to dimensional dispersions in all specimens. The fact that dimensional dispersions were mainly from surface roughness and not variability in the fabrication processes is a testament to the specimen-to-specimen reproducibility of the process flow. Parametric monitoring during fabrication with this reticle set generated an average h of 2.33 μm.

The fracture behavior was characterized using the F_{app}-t profiles (figure 2(c)) during mechanical testing and high-resolution SEM images (insets in figures 2(d)–(g)) of the shoulder fillets after mechanical testing. From the F_{app}-t trace, it is clear that the loading behavior was linear, implying brittle failure by the propagation of a single crack. On occasion, multiple specimens broke simultaneously or a single specimen broke outside the shoulder fillet and gauge sections, leading to large erratic excursions or aberrant F_f values in the F_{app}-t trace, respectively. Such anomalous behavior was attributed to shock transmission between specimens during fracture and premature failure in other sections of the slack-chain; the corresponding data were omitted from further analyses. From the high-resolution SEM images, it was found that failure typically occurred at or near the shoulder fillet region. More specifically, the S1 and S2 specimens failed solely in the shoulder fillet region, while the failure region for the S3 and S4 specimens extended into the small gauge section. Fractography of broken specimens revealed that fracture initiated at sidewall surface features that were likely formed from preferential etching of grain boundaries [4–6, 10]. Furthermore, the fracture surfaces exhibited hackle lines and preferred cleavage planes, typical features for polysilicon [2, 4] and single-crystal silicon [22, 23].

3.2. Force, stress, and strength distributions

The component failure force edfs $P(F_f)$ for the four different specimen geometries are shown in figure 3(a). The symbols represent fracture force values from individual specimens. The failure force edf curves were sigmoidal in shape and clearly distinguishable. For a given $P(F_f)$, the F_f quantiles (e.g. median) decreased in the following specimen order: S4, S2, S1, and S3. In other words, the F_f values decreased initially as D increased at a constant d and then again as d decreased. The stress edfs $P(\sigma_g)$ for the four different specimen geometries are shown in figure 3(b). Again, the symbols represent gauge section stress values from individual specimens. The stress edf curves were distinguishable, but rearranged, with respect to figure 3(a). For a given $P(\sigma_g)$, σ_g decreased in the following specimen order: S4, S3, S2, and S1. As such, the σ_g at failure decreased as SCF increased. Finally, the fracture strength edfs $P(\sigma_f)$ for the four different specimen geometries are shown in figure 3(c). The strength edfs were reordered with respect to figures 3(a) and (b), such that the σ_f curves for the S1 and S2 specimens were nearly identical, but then shifted to smaller σ_f values for the S3 and S4 specimens.

Two important trends are clear from figure 3(c): (1) The minimum strength of each distribution was invariant, such that changes in specimen geometry led to a contraction of distributions towards the minimum and (2) The distribution contraction was greater (i.e. the width of the distribution was smaller) as the specimen SCF decreased. Both trends are explained via 'weakest-link' arguments, in which a chain (several elements in a component) is only as strong as its weakest link (a single element from the population) [8]. Both component and population strength distributions are terminated by a single threshold strength associated with the maximum flaw size. As such, the threshold strength is invariant with the number of links in the chain, or more explicitly, the size of the component. For large components, there is a large probability that most components in a group contain flaws of near maximum size and thus the group exhibits a contracted strength distribution adjacent to the threshold. As component size decreases, the probability increases that some components contain strength-controlling flaws smaller than the maximum size and the strength distribution broadens. The inference from figure 3(c) is that the broad, nearly identical strength distributions for the S1 and S2 specimens are consistent with similar, small effective component sizes and the contracted distributions for the S3 and S4 specimens are consistent with larger effective sizes.

3.3. Flaw size distribution and length scaling factors

The flaw size distribution was calculated from the $P(\sigma_f)$ strength response of the S1 specimens in figure 3(c). In more detail, $f(c)$ was determined from the $F(\mu)$ best fits to the $P(\sigma_f)$ data, using $B = 0.75$ MPa m$^{1/2}$ for silicon [7] and equations

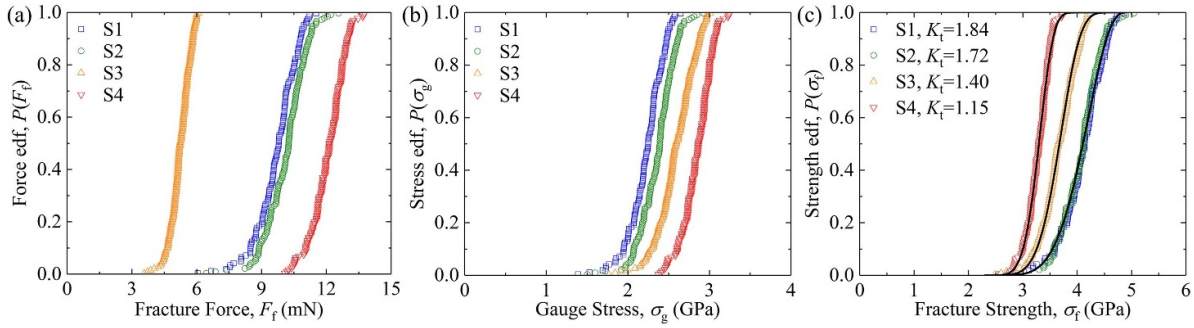

Figure 3. Force, stress, and strength distributions. (a) $P(F_f)$, (b) $P(\sigma_g)$, and (c) $P(\sigma_f)$ for the four different specimen geometries. The symbols represent individual tests and the lines represent best fits to the data using equation (1) for the S1 specimens and equation (8) with L_n/L_1 as the fitting parameter for the S2, S3, and S4 specimens.

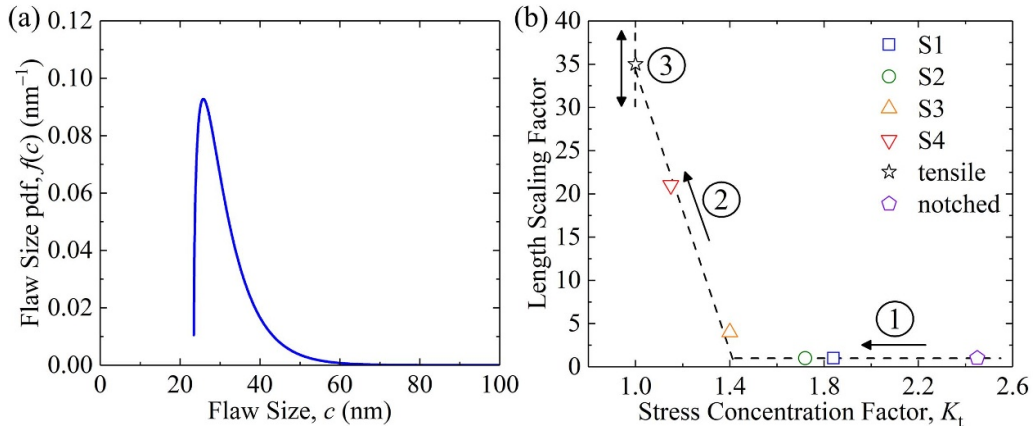

Figure 4. Flaw size distribution and length scaling factors. (a) $f(c)$ pdf from the best fit to the data for the S1 specimens with $\Delta L/L_1 = 1/2$. (b) Length scaling factors as a function of stress concentration factors. SCFs were determined with the body force method and L_n/L_1 were calculated with best fits to the strength data for the S2, S3, and S4 specimens. Tensile ($K_t = 1$) and notched ($K_t = 2.45$) data are also shown for reference.

Table 2. Stress concentrations and length scaling factors for the four shoulder fillet geometries. SCFs were determined using both a body force method and FEA, whereas L_n/L_1 were calculated using best fits to the strength data for the S2, S3, and S4 specimens.

Specimen Type	Body Force Method SCF, K_t	Finite Element Analysis SCF, K_t	Length Scaling Factor L_n/L_1
S1	1.84	1.86	–
S2	1.72	1.77	1
S3	1.40	1.42	4
S4	1.15	1.15	21

(3)–(5) with $\Delta L/L = 1/2$. The resulting flaw-size pdf $f(c)$ is shown in figure 4(a). The pdf is asymmetric, consisting of a prominent peak at flaw sizes ranging from 20 nm to 30 nm and an extended tail to sizes of 70 nm. The asymmetric character of the distribution in figure 4(a) is in good agreement with previous studies on flaw populations in micro- and nano-scale silicon components [4, 8, 10] and other ceramic materials [9]. The asymmetry in the pdf derives physically from the fact that $c \sim \sigma^{-1/2}$ as dictated by equation (4) and is enhanced mathematically by taking the derivative to form the pdf from the cdf as defined by equation (5). The domain of flaw sizes is nearly equivalent to results from another reticle set for the poly3 layer [10], demonstrating reticle-to-reticle reproducibility in the fabrication process.

The length scaling factors were evaluated from the $P(\sigma_f)$ data for the S2, S3, and S4 specimens in figure 3(c). More specifically, the $P(\sigma_f)$ data for the S2, S3, and S4 specimens were fit to equation (8), using the fit for S1 specimens from equation (1) as a basis and L_2/L_1, L_3/L_1, and L_4/L_1 as the fitting parameters. The lines in figure 3(c) represent the best fits to the data and describe the strength variations well over the entire range, consistent with the existence of a single flaw population in all of the shoulder fillet specimens. The resulting length scaling factors are shown in figure 4(b) and listed in table 2, both as a function of the SCF values from the body force method calculations. In general, it was found that the length scaling factor was initially constant and then increased as SCF decreased. The change in trend is related to a change

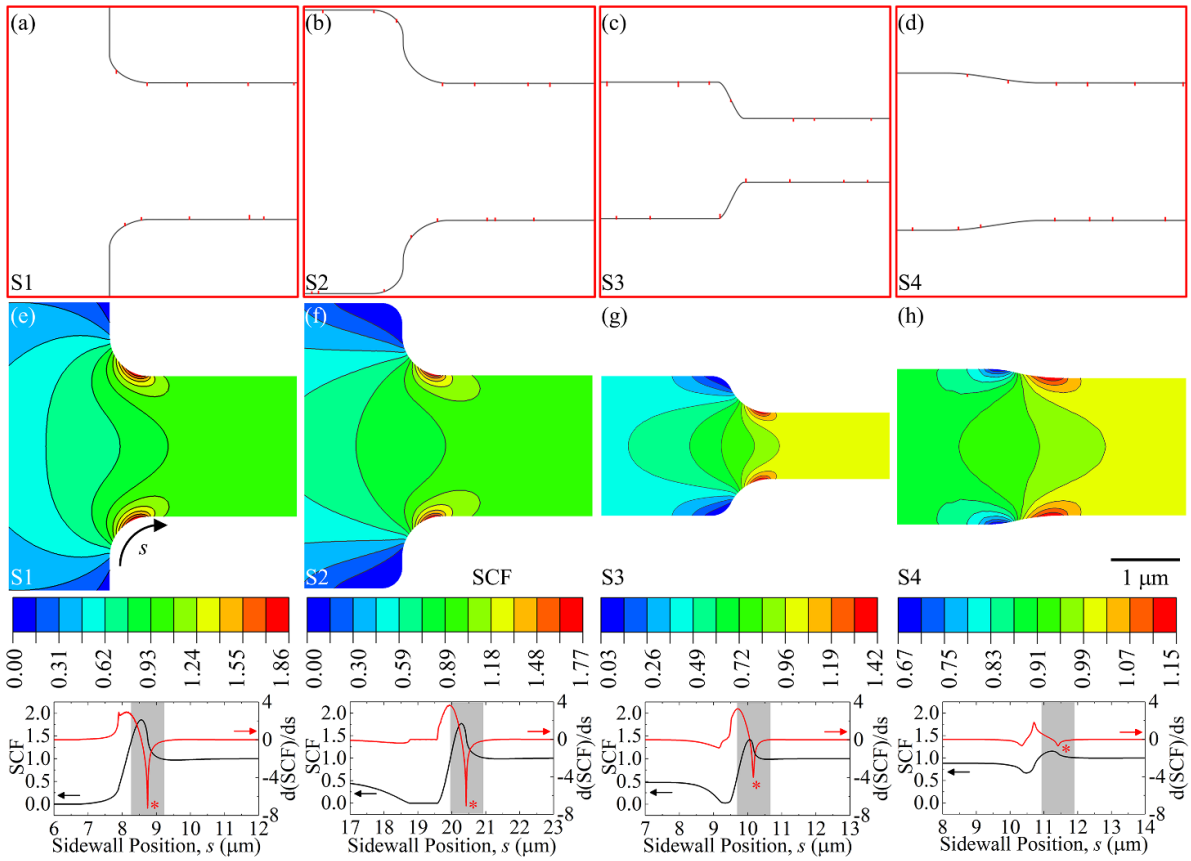

Figure 5. Monte Carlo and FEA simulations. (a)–(d) Monte Carlo simulations of the flaw size and spacing distributions in the shoulder fillet regions for the (a) S1, (b) S2, (c) S3, and (d) S4 specimens. Flaw sizes and spacings were selected randomly from $f(c)$ and a uniform ΔL distribution, respectively. (e)–(h) FEA of the shoulder fillet regions for the (e) S1, (f) S2, (g) S3, and (h) S4 specimens. The minimum width sections were loaded with unit stress so the maximum principal stress contours were identical to SCFs. SCFs (black lines) and changes in SCFs with position (red lines) were plotted along the sidewall surfaces.

in the stress concentrating effects of the shoulder fillets and can be described in terms of the three regions shown in figure 4(b). In region 1 ($K_t \geq 1.4$), $L_2/L_1 = 1$, suggesting the SCF is large enough to ensure failure from a single flaw on one of the two shoulder surfaces. The notched bars from previous work fall into the upper end of this regime [10], whereas the S1 and S2 shoulder fillet specimens presented here fall into the lower end of this regime. In region 2 ($1.0 < K_t < 1.4$), the SCF decreases to less than a threshold value, such that the length scaling factor increases to $L_3/L_1 = 4$ for S3 specimens and $L_4/L_1 = 21$ for S4 specimens. These increases suggest that a decrease in SCF extends the effective length over which strength-limiting flaws are active. The trend continues until the shoulder fillets are completely removed; previous work reported a length scaling factor of 35 for poly3 tensile bars [10]. In region 3 ($K_t = 1.0$), the length scaling factor can decrease or increase with the length of the tensile bar, approaching 1 as $L \to \Delta L$ and ∞ as $L \to \infty$.

3.4. Monte Carlo and FEA simulations

The schematic diagrams in figures 5(a)–(d) represent the surfaces of the shoulder fillet regions as determined from the Monte Carlo simulations. The shoulder fillet outlines were created from the nominal dimensions in table 1, and perturbed using flaw sizes selected randomly from the $f(c)$ distribution in figure 4(a) and flaw spacings selected randomly from a uniform ΔL distribution (0.57 μm $\pm$ 0.48 μm). The scaled diagrams facilitate a quantitative assessment of the *flaw size distribution and length scaling factors* relative to specimen geometry. For the flaw size distribution, the pdf was asymmetric, exhibiting a prominent peak at sizes between 20 nm to 30 nm and an extended tail to 70 nm as shown in figure 4(a). Hence, the values of c were only a few percent of the mean values of d for all four geometries, and therefore represented only a small reduction in the minimum width. For the length scaling factors, the factor was initially constant and then increased as SCF decreased as shown in figure 4(b). For S2 specimens, $\Delta L \approx \pi R/2$ and $L_2/L_1 = 1$, suggesting that the average flaw spacing was nearly equivalent to the shoulder fillet arc length (i.e. on average, there was only a single flaw on each fillet) and failure initiated at one of these two flaws (i.e. due to the enhanced SCFs in the fillets). For S3 specimens, $\Delta L \approx \pi R/2$ and $L_3/L_1 > 1$, indicating that there was still only a single flaw on each fillet, but that fracture was not limited to these flaws (i.e. the effective length of the specimen extended beyond the shoulder fillet into the minimum gauge width). This

increase in length was responsible for the occasional failure in the small gauge section as shown in figure 2(f) and the smaller σ_f values in figure 3(c). For S4 specimens, $\Delta L < \pi R/2$ and $L_4/L_1 > 1$. In this case, there were numerous flaws on each fillet and the effective length extended well beyond the shoulder fillet region. This triggered failures in the minimum gauge section and contracted the σ_f distribution to even smaller values.

The contour maps in figures 5(e)–(h) represent the maximum principal stresses (or the SCFs, given that the minimum width sections were loaded axially with unit stress) in the shoulder fillet regions as determined via FEA simulations. The contour maps facilitate a quantitative assessment of the *stress distributions* relative to specimen geometry. From the maps, it was clear that all four geometries had stress concentrations in the shoulder fillet regions, with the magnitude of the concentrations dependent on the specimen geometry. The maximum SCFs from the FEA simulations are shown in table 2. The data suggested that SCF decreased as the geometry changed from the S1 to the S4 specimen. In fact, results from the FEA simulations were in excellent agreement with those from the body force method; the mean values in K_t were found to be statistically similar given the uncertainties in K_t from dimensional dispersions [10] and numerical errors [16]. SCF traverses along the sidewall surfaces as a function of position s are also shown in figures 5(e)–(h). Both SCFs (black lines) and derivatives of SCFs with s (red lines) are shown. The gray bands are common to each plot, indicate the largest likely flaw separation in these specimens ($\approx$0.96 μm), and are centered on the derivative maximum. The SCF derivative trends in comparison with the flaw separations showed that certain aspects of the rate of change in SCF with s correlated well with the length scaling factor trends. In particular, the width of the derivative peak was initially well contained in the flaw separation band for the S1 and S2 specimens and then spread beyond this band for the S3 and S4 specimens. The significant increases in SCF for the S1 and S2 specimens localized fracture to the shoulder fillet regions (i.e. $L_2/L_1 = 1$), while the gradual decreases in SCF for the S3 and S4 specimens increased the likelihood of failure in the minimum width section (i.e. $L_4/L_1 > 1$).

4. Discussion

A major goal of this work was to provide a clear linkage between the requirements of the MEMS designer and the MEMS fabricator. Designers require different distributions of sustainable forces for MEMS components of various geometries. Fabricators require methods to optimize material intensive distributions of strength-controlling flaws in MEMS components from identical processing. The goal of linking these two requirements was demonstrated here using the failure characteristics of polysilicon MEMS components with various fillet geometries formed into sequential chain tensile test structures in identical processing steps. The fillet geometries generated a range of stress concentration effects that provided an intermediate gradation between the extremes of the notched and smooth bar tensile geometries studied earlier [10]. In addition to demonstrating the connection between failure force and flaw distributions mediated by component geometry (section 3 above), the range of geometries also verified and extended the earlier analyses (see discussion above and figure 4(b)). Physically, the demonstrations were in accordance with physical intuition: (1) Smaller components with large stress concentrations exhibited smaller failure force distributions that were well separated from the failure force distributions of large components with small stress concenrations and (2) Geometry effects were manifest as contractions of strength distributions adjacent to a minimum strength threshold common to all components, consistent with weakest-link arguments.

Mathematically, the demonstration implements an analysis in which the key independent elements can be clearly identified. Combining the above equations enables the distribution of failure forces for a group of components of fixed geometry $H(F_f)$ to be expressed in terms of the underlying invariant flaw population $f(c)$

$$H(F_f) = 1 - \left[\int_{c_{min}}^{(BA/K_tF_f)^2} f(c)\,dc\right]^{L/\Delta L}. \tag{9}$$

The fracture resistance of the material and the nature of the flaw are encapsulated in B: for simple Griffith flaws, B can be identified with the material toughness. The size of the component is encapsuslated in A, an effective gauge cross-sectional area, and L, an effective gauge length. The shape of the component is encapsulated in K_t, the SCF of the most extreme variation of component outline. The flaw population is encapuslated in the minimum flaw size c_{min}, the flaw size pdf $f(c)$, and the average flaw spacing ΔL. The bounds on the domain of $H(F_f)$, $F_{min} \leqslant F_f \leqslant F_{max}$, depend on the fracture resistance parameter B, and inversely on the bounds on the flaw population c_{min} and c_{max}, as does strength [8–10]. Distinct from strength, the failure forces also depend on component geometry parameters A and K_t as

$$F_{min} = BA/K_tc_{max}^{1/2}, \tag{10}$$

and

$$F_{max} = BA/K_tc_{min}^{1/2}. \tag{11}$$

As a consequence, although the strength domain is intensive and strength distributions contract to a fixed threshold as component geometry is varied (figure 3(c)), the failure force domain is extensive and varies with component geometry (figures 3(a) and (b)). Fabrication choices determine B, $f(c)$, and ΔL. Design choices determine A, L, and K_t. Equations (9)–(11) make the engineering linkage explicit in the determination of failure forces. Proof testing artificially engineers $f(c)$ through non-fabrication means by exposing components to $F_{proof} > F_{min}$, such that the flaw population is truncated at $c_{proof} < c_{max}$ [24].

It is important to note that as $f(c)$ is specified separately from the specimen size parameters A and L in equation (9), any flaw population function can be used to describe size effects,

including common descriptions such as the Weibull, normal, and (as here) Beta functions. This point has been discussed in detail by Zok [25] and elsewhere [8]. It is also important to note that the exponent in equation (9) is specified separately from the terminals of the integral, such that any relationship between flaw size and strength, including non-linear and (as here) linear fracture mechanics relations, will exhibit a size effect. This point was briefly considered by Reedy *et al* [5] and elsewhere [9]. As a consequence of this separate specification, it is implicit in developing equation (9) that all flaws in a test component are exposed to the same stress and stress concentration. This condition may not be so in large-grained materials or materials with wide grain size distributions, in which elastic anisotropy and balances between intergranular and transgranular fracture may influence the values of K_t and B from specimen to specimen. This effect has been studied by Corigliano and colleagues [26, 27]. Similarly, it is implicit in equation (9) that all specimens contain the same density of flaws, that is, that ΔL is fixed for a sample group. If ΔL varies from specimen to specimen, the failure load distribution of the sample group $H(F_f)$ is perturbed, although the threshold remains fixed. This effect has been studied by Xu *et al* [28]. Forward analyses of flaw populations can show this easily, but reverse analyses of strength distributions (as here) cannot discern the effect as experimental strengths only sense the single, largest flaw in an entire specimen without regard for flaw density. More broadly, although the experimental data support the assumption of flaw independence imbedded in equation (3) leading to equation (9)—widely separated small flaws [8–10]—this is certainly an issue for small-scale MEMS components and has been considered by Xu *et al* [28] and Todinov [29].

5. Conclusions

An analytical framework developed to describe the strengths of smooth and notched MEMS tensile bars is applicable to the failure forces of stepped bars with shoulder fillets. A critical element in the application is the use of the correct SCFs for the fillet geometries. Here, SCFs determined by an analytical body force method were verified by FEA, providing confidence in application of the analytical SCF expressions to other MEMS components in which the common and critical shoulder fillet geometry is failure controlling. The extension of the weakest-link-based framework to another geometry provides further empirical support for the mathematical structure and the linkages and distinctions between flaw populations and sampled strength distributions. An additional critical element in the overall failure force prediction procedure is the ability to measure the detailed shape and location of strength distributions: High throughput test methods applied to identically-fabricated specimens provide such an ability and was demonstrated here with the slack-chain geometry capable of measuring strengths of hundreds of specimens. Lastly, it was found that the shoulder fillet radii for polysilicon components were markedly larger that those previously reported for single-crystal silicon due to differences in the fabrication processes. The larger r result in smaller SCFs for similar designs, suggesting that parametric studies linking fabrication parameters to component geometry are required to fully elucidate the load bearing ability of MEMS. In all, MEMS failure prediction is well advanced, both analytically and experimentally, and has overcome many of the limitations [7] noted previously.

Acknowledgments

B.L.B. was supported by the Center for Integrated Nanotechnologies, a Department of Energy office of Basic Energy Sciences user facility. Sandia National Laboratories is a multimission laboratory managed and operated by National Technology and Engineering Solutions of Sandia LLC, a wholly owned subsidiary of Honeywell International Inc., for the U.S. Department of Energy National Nuclear Security Administration under contract DE-NA0003525. The views expressed in the article do not necessarily represent the views of the U.S. Department of Energy, U.S. Department of Defense, or U.S. Government. Certain commercial equipment, instruments, and software are identified in this paper in order to specify the experimental procedure adequately. Such identification is not intended to imply recommendation or endorsement by NIST, nor is it intended to imply that the equipment or software identified are necessarily the best available for the purpose.

ORCID iDs

Frank W DelRio
https://orcid.org/0000-0003-1727-8220
Lawrence H Friedman
https://orcid.org/0000-0003-2416-9903
Robert F Cook
https://orcid.org/0000-0003-0422-8881

References

[1] Manners D 2018 MEMS to take 73% of sensor market this year *Electronics Weekly.com*
[2] Boyce B L 2010 A sequential tensile method for rapid characterization of extreme-value behavior in microfabricated materials *Exp. Mech.* **50** 993–7
[3] Chasiotis I and Knauss W G 2003 The mechanical strength of polysilicon films: part 1. The influence of fabrication governed surface conditions *J. Mech. Phys. Solids* **51** 1533–50
[4] Boyce B L, Grazier J M, Buchheit T E and Shaw M J 2007 Strength distributions in polycrystalline silicon MEMS *J. Micro. Syst.* **16** 179–90
[5] Reedy E D, Boyce B L, Foulk J W, Field R V, de Boer M P and Hazra S S 2011 Predicting fracture in micrometer-scale polycrystalline silicon MEMS structures *J. Micro. Syst.* **20** 922–32
[6] Saleh M E, Beuth J L and de Boer M P 2014 Validated prediction of the strength size effect in polycrystalline silicon using the three-parameter Weibull function *J. Am. Ceram. Soc.* **97** 3982–90

[7] DelRio F W, Cook R F and Boyce B L 2015 Fracture strength of micro- and nanoscale silicon components *Appl. Phys. Rev.* **2** 021303–1–51
[8] Cook R F and DelRio F W 2019 Material flaw populations and component strength distributions in the context of the Weibull function *Exp. Mech.* **59** 279–93
[9] Cook R F and DelRio F W 2019 Determination of ceramic flaw populations from component strengths *J. Am. Ceram. Soc.* **102** 4794–808
[10] Cook R F, DelRio F W and Boyce B L 2019 Predicting strength distributions of MEMS structures using flaw size and spatial density *Microsyst. Nanoeng.* **5** 49–1–12
[11] Cook R F 2006 Strength and sharp contact fracture of silicon *J. Mater. Sci.* **41** 841–72
[12] DelRio F W, Friedman L H, Gaither M S, Osborn W A and Cook R F 2013 Decoupling small-scale roughness and long-range features on deep reactive ion etched silicon surfaces *J. Phys. D: Appl. Phys.* **114** 113506–1–6
[13] Hankins M G, Resnick P J, Clews P J, Mayer T M, Wheeler D R, Tanner D M and Plass R A 2003 Vapor deposition of amino-functionalized self-assembled monolayers on MEMS *Proc. SPIE* **4980** 238–47
[14] LaVan D A, Tsuchiya T, Coles G, Knauss W G, Chasiotis I and Read D 2001 Cross comparison of direct strength testing techniques on polysilicon films *ASTM Spec. Tech. Publ.* **1413** 16–27
[15] Noda N A, Takase Y and Monda K 1997 Stress concentration factors for shoulder fillets in round and flat bars under various loads *Int. J. Fatigue* **19** 75–84
[16] Noda N A and Takase Y 2004 Stress concentration factor formulas useful for any dimensions of shoulder fillet in a flat test specimen under tension and bending *J. Test. Eval.* **32** 217–26
[17] Pilkey W D and Pilkey D F 2008 *Peterson's Stress Concentration Factors* 3rd edn (New York: Wiley)
[18] Lawn B R 1993 *Fracture of Brittle Solids* 2nd edn (Cambridge: Cambridge University Press)
[19] Gaither M S, Gates R S, Kirkpatrick R, Cook R F and DelRio F W 2013 Etching process effects on surface structure, fracture strength, and reliability of single-crystal silicon theta-like specimens *J. Micro. Syst.* **22** 589–602
[20] ABAQUS . 2019. Dassault Systèmes
[21] Suwito W, Dunn M L, Cunningham S J and Read D T 1999 Elastic moduli, strength, and fracture initiation at sharp notches in etched single crystal silicon microstructures *J. Appl. Phys.* **85** 3519–34
[22] Gaither M S, DelRio F W, Gates R S, Fuller E R and Cook R F 2010 Strength distribution of single-crystal silicon theta-like specimens *Scr. Mater.* **63** 422–5
[23] Gaither M S, DelRio F W, Gates R S and Cook R F 2011 Deformation and fracture of single-crystal silicon theta-like specimens *J. Mater. Res.* **26** 2575–89
[24] Boyce B L, Ballarini R and Chasiotis I 2008 An argument for proof testing brittle microsystems in high-reliability applications *J. Micromech. Microeng.* **18** 117001–1–4
[25] Zok F W 2017 On weakest link theory and Weibull statistics *J. Am. Ceram. Soc.* **100** 1265–8
[26] Corigliano A, Ghisi A, Langfelder G, Longoni A, Zaraga F and Merassi A 2011 A microsystem for the fracture characterization of polysilicon at the micro-scale *Eur. J. Mech.* A **30** 127–36
[27] Mariani S, Martini R, Ghisi A, Corigliano A and Simoni B 2011 Monte Carlo simulation of micro-cracking in polysilicon MEMS exposed to shocks *Int. J. Fract.* **167** 83–101
[28] Xu Z, Ballarini R and Le J-L 2019 A renewal weakest-link model of strength distribution of polycrystalline silicon MEMS structures *J. Appl. Mech.* **86** 081005–1–10
[29] Todinov M T 2009 Is Weibull distribution the correct model for predicting probability of failure initiated by non-interacting flaws? *Int. J. Solids Struct.* **46** 887–901